



A comparative study of different features extracted from electrochemical impedance spectroscopy in state of health estimation for lithium-ion batteries

Bo Jiang^{a,b}, Jiangong Zhu^b, Xueyuan Wang^{c,d,*}, Xuezhe Wei^{b,d}, Wenlong Shang^e, Haifeng Dai^{b,d,*}

^a Postdoctoral Station of Mechanical Engineering, Tongji University, Shanghai 201804, China

^b School of Automotive Studies, Tongji University, Shanghai 201804, China

^c Department of Control Science and Engineering, Tongji University, Shanghai 201804, China

^d Clean Energy Automotive Engineering Center, Tongji University, Shanghai 201804, China

^e Beijing Key Laboratory of Traffic Engineering, College of Metropolitan Transportation, Beijing University of Technology, Beijing 100124, China

HIGHLIGHTS

- An in-depth analysis of feature extraction from EIS is provided for SOH estimation.
- Three features in SOH estimation are constructed using knowledge of battery EIS.
- The Gaussian process regression is employed to realize the battery SOH estimation.
- A comprehensive assessment of EIS features in SOH estimation is carried on.
- The proposed SOH estimation is adaptive to different aging conditions.

ARTICLE INFO

Keywords:

Lithium-ion battery
State of health
Electrochemical impedance spectroscopy
Comparative study
Data-driven

ABSTRACT

Battery state of health (SOH) estimation is a critical but challenging demand in advanced battery management technologies. As an essential parameter, battery impedance contains valuable electrochemical information reflecting battery SOH. This study investigates a systematic comparative study of three categories of features extracted from battery electrochemical impedance spectroscopy (EIS) in SOH estimation. The three representative features are broadband EIS feature, model parameter feature, and fixed-frequency impedance feature. Based on the deduced EIS features, a machine learning technique using Gaussian process regression is adopted to estimate battery SOH. The battery aging and electrochemical tests for commercial 18650-type batteries are performed, in which the constant and dynamic discharging conditions are considered during battery aging. The battery life-cycle capacity and EIS data are collected for the machine learning model. The performance of the constructed features is investigated and comprehensively compared in terms of estimation accuracy, certainty, and efficiency. Experimental results highlight that using the fixed-frequency impedance feature can realize outstanding performance in battery SOH estimation. The average of the maximum absolute errors for different cells under different aging conditions is within 2.2%.

1. Introduction

Lithium-ion batteries (LIBs) have been massively serviced in electric vehicles and energy storage systems due to their outstanding performance [1]. However, as electrochemical devices, LIBs face the problems

of environmental sensitivity, inevitable aging, and thermal safety [2,3]. To ensure the effective utilization of LIBs, advanced battery management technologies play a critical role [4]. State estimation is one of the critical and challenging tasks in battery management technologies [5], which indicates detailed battery information from the aspects of

* Corresponding authors.

E-mail addresses: 7wangxueyuan@tongji.edu.cn (X. Wang), tongjidai@tongji.edu.cn (H. Dai).

<https://doi.org/10.1016/j.apenergy.2022.119502>

Received 10 January 2022; Received in revised form 9 June 2022; Accepted 17 June 2022

Available online 24 June 2022

0306-2619/© 2022 Elsevier Ltd. All rights reserved.

electrical, thermal, and aging characteristics. Battery health state (also known as the state of health, SOH), usually reflected from the battery capacity and impedance, is defined to assess the aging level quantitatively. However, battery SOH cannot be conveniently obtained through direct measurement during vehicle application. Therefore, many efforts have been put into exploring and improving the battery health state estimation. Generally, the health state estimation approaches can be divided into two categories: model-based estimation and data-driven-based estimation [5,6].

The battery model is the prerequisite of the model-based estimation methods, in which the physics-based electrochemical model and equivalent circuit model (ECM) are two commonly used battery models [7]. The physics-based electrochemical model is used to estimate the health state from the perspective of battery degradation mechanisms [8]. Xiong et al. [9] studied an electrochemical model and concluded that five characteristic parameters are highly related to battery degradation; further, a battery health state estimation was developed based on these five parameters. Considering that the solid electrolyte interphase (SEI) layer formation and lithium plating are the main aging factors, Bi et al. [10] constructed a high-fidelity physics-based electrochemical model and employed a particle filter to realize the online SOH and aging parameter estimation. Compared with the electrochemical model, the ECMs are more concise, and some adaptive filters have been employed to estimate battery capacity or SOH with the assistance of battery ECMs [11]. However, the simple model structure is difficult to reflect the complex battery mechanism, which is challenging to ensure accurate health estimation over the whole life-cycle.

With the development of artificial intelligence and machine learning, data-driven estimation techniques have become the research highlights among battery health state estimation, based on the relevance between battery states and related features. Generally, the adopted machine learning technique and selected data feature significantly influence the state estimation performance. Support vector regression [12], Gaussian process regression (GPR) [13,14], and random forest regression [15] are commonly used techniques in traditional machine learning. Recently, neural network techniques, especially the deep neural network, have become an effective tool in battery technologies [16]. The representative networks include the long short-term memory network [17] and gated recurrent unit network [18].

As fundamental and direct measurements, battery voltage and current are preferred to generate the data features. Moreover, onboard battery charging usually adopts the constant current-constant voltage (CC-CV) charging pattern, which is more stable than the dynamic battery discharging condition. Hu et al. [19] extracted five battery characteristic features from the complete charging curve, including initial charging voltage, charging capacity during constant current (CC) and constant voltage (CV) phase, and final charging voltage and current. Besides these features, the curvature radius of the charging current curve during the CV phase was also regarded as the data feature for battery SOH estimation [20]. With the development of deep learning techniques, the processed feature dimension increases. Shen et al. [21] divided the battery charging process into 25 segments, and the voltage, current, and charging capacity of each segment were used as the input of the machine learning algorithm. Similarly, Li et al. [22] converted the charging time series data into three-dimensional images, regarded as the input of the convolutional neural network. Higher-dimensional features carry more valuable information from battery charging data and improve the estimation performance; nevertheless, the computational burden will also increase accordingly. Nevertheless, the above research focuses on SOH estimation from stable and specific charging conditions, while the battery operating profiles in the real applications are more dynamic, complex and time-varying, challenging the feature engineering process of existing approaches [23,24]. To address this problem, Zhang et al. [24] proposed a machine learning-based approach for battery aging prediction using the histogram data feature, and an online adaptation strategy was investigated for individual cell characteristics.

The proposed framework has shown good performance even with randomized discharging data and real-world fleet data. Deng et al. [25] reconstructed the dynamic discharging profiles and found that the standard deviation of discharge capacity differences is strongly correlated to battery aging; further, an adaptive battery SOH estimation method was proposed.

Battery electrochemical impedance spectroscopy (EIS) containing important battery information has shown a vital role in battery management technologies [26,27]. Currently, the onboard measurement of battery electrochemical impedance has become a reality, and some advanced and practical methods have been proposed [28,29]. At present, impedance is frequently reported for battery state of charge (SOC) estimation [30], temperature estimation [31,32], capacity estimation [33], remaining useful life prediction [34], degradation mode identification [35], lithium plating detection [36,37], etc. Inspired that the traditional data-driven techniques using the battery charging features, some researchers attempted to extract features from EIS for health estimation. Generally, as indicated in Fig. 1, three categories of feature extraction methods are summarized from existing literature.

Feature extracted from broadband EIS: After obtaining the battery EIS, the most direct approach is to utilize the impedance data at all frequency points, as shown in Fig. 1 (a). Zhang et al. [33] constructed a data-driven model with the input dimension of 120 (60 frequencies), further realizing the battery capacity estimation and life prediction. However, this study used the coin cell as the experiment object, and the effectiveness of this kind of EIS feature for traction batteries needs to be further investigated. Based on the dataset provided by Zhang et al. [33], Xu et al. [38] built a hybrid feature composed of features extracted from broadband EIS and incremental capacity, further adopting the extreme learning machine for capacity estimation. To avoid the influence of high dimensional input on computational cost, Fu et al. [39] determined to utilize six representative features for battery SOH estimation, including the peak value of impedance imaginary part, as well as the real part and amplitude at the corresponding frequency point, and the peak value of impedance phase.

Feature extracted from model parameter: This kind of feature extraction approach is based on battery ECM, which needs to obtain the model parameters from the EIS data first, as presented in Fig. 1 (b). Resistors, constant phase elements (CPEs), and Warburg elements are common elements in the ECM for battery EIS analysis. By analyzing the changing tendency over the life-cycle, the SEI resistance [40], charge transfer resistance [41], and diffusion CPE [42] are adopted to assess the battery health state. Moreover, the estimation model constructed by Wang et al. [41] considered the battery temperature and SOC, making the estimation more applicable and practical. Considering that the relaxation effect has a significant impact on battery EIS, Messing et al. [43] investigated the variation characteristic of battery equivalent resistance during short-term relaxation time, further establishing a rapid SOH estimation method.

Feature extracted from fixed-frequency impedance: Different from the model parameter feature, a more practical and easier to implement approach is constructing the relationship between battery aging and a fixed-frequency impedance feature. Locorotondo et al. [44] found that there may be a certain frequency point that can distinguish battery SOH through data clustering, even though battery EIS is tested with different SOCs and excitation current. Besides, by using the automatic relevance determination technique, Zhang et al. [33] concluded that the EIS feature at a specific frequency shows greater importance than features at other frequencies in battery capacity estimation, which can avoid the measurement of battery EIS over a broad range of frequencies.

Based on the above discussion, feature extraction methods in battery EIS are critical for health assessment throughout the life-cycle. Therefore, it is necessary to analyze the performance of representative feature extraction methods for battery impedance, which is still a blank area of SOH estimation research. Given this, this study intends to bridge the

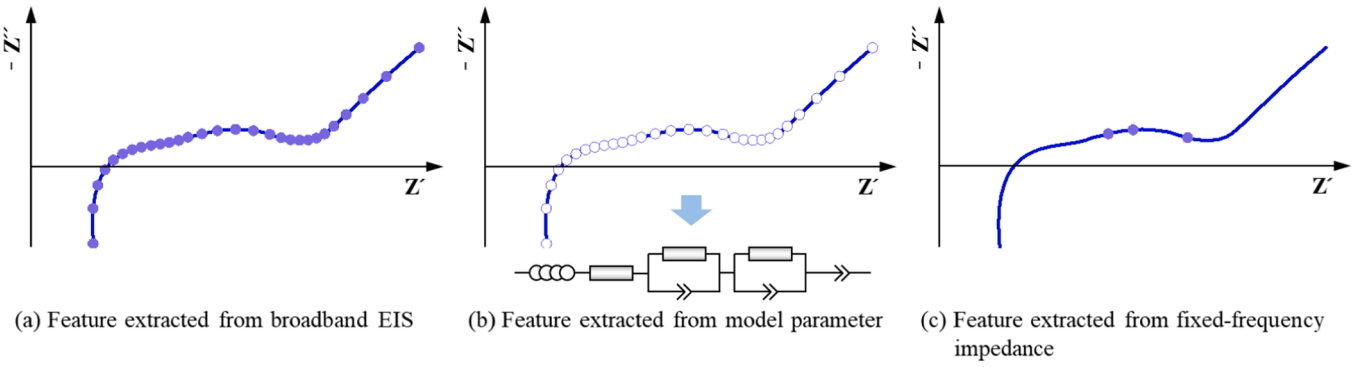


Fig. 1. The diagram of three categories of feature extraction methods.

research gap by systematically assessing and analyzing the performance of these feature extraction methods, including estimation accuracy, confidence, and efficiency. This comparative study is expected to provide an in-depth analysis of feature extraction methods in battery state estimation and help battery management engineers develop the most appropriate feature extraction and estimation methods. The main contributions are summarized as follows: (1) The life-cycle battery capacity fading and electrochemical tests for commercial 18650-type batteries are performed, and then a battery EIS dataset is constructed. The dynamic discharging condition is considered during the battery cycling aging test, which is closer to the actual battery operation conditions. (2) Three feature extraction approaches from battery EIS for SOH estimation are constructed using knowledge of battery impedance. A data-driven approach based on the GPR model is constructed to realize battery SOH estimation using the deduced data features from battery EIS. Three kinds of performance metrics are introduced to evaluate the performance of each data feature. (3) Following the procedure of the multiple-test, a comprehensive assessment of each EIS feature in terms

of SOH estimation accuracy, certainty, and efficiency is carried on. Furthermore, a systematic comparison between three EIS features is performed, and it can be concluded that using the proper frequency point as the data feature can achieve comprehensively outstanding performance in battery SOH estimation.

The remainder of this study is organized as follows. Section 2 details the battery experimental setup and testing schedule, followed by the description of the established EIS dataset. The fundamental techniques of the battery health estimation based on three kinds of EIS features are presented in Section 3. Section 4 discusses the performance of each EIS feature in battery SOH estimation, then an in-depth comparison between these EIS features is performed. Finally, Section 5 concludes this study.

2. Battery experiments and dataset description

This section first introduces the experimental setup to perform the battery aging and electrochemical tests, followed by the designed aging schedule. This section also provides a detailed description of the

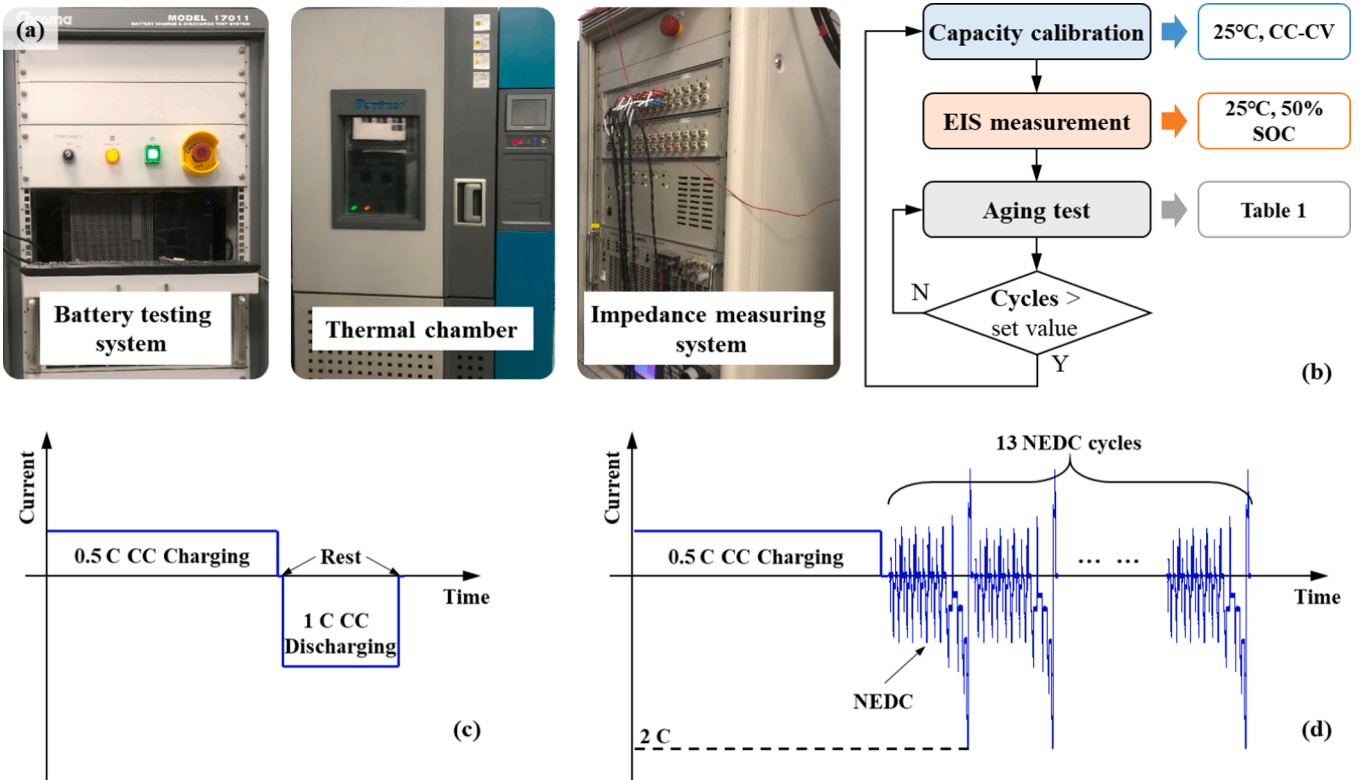


Fig. 2. Experimental setup and battery testing schedule: (a) Test bench; (b) Test procedure; (c) The aging test profile for Cell 1 and Cell 3; (d) The aging test profile for Cell 2 and Cell 4.

obtained dataset to investigate the data-driven models.

2.1. Experimental setup

To obtain the battery fading data and corresponding impedance, a battery experimental setup, as shown in Fig. 2 (a), is established. The experimental setup consists of a battery testing system (Chroma 17011) for battery aging experiments and capacity calibration, a multi-channel impedance measuring system (TOYO TA500) for battery impedance spectrum measurement, and a thermal chamber to control the ambient temperatures. This study employed commercially available Samsung INR18650-29E cells with the Li(NiCoAl)O₂ cathode and graphite anode. The charging and discharging cut-off voltages are 4.2 V and 2.5 V, respectively. The nominal capacity is 2.75Ah. Before experiments, a consistency check test is performed, in which the difference of initial capacity is within 1% among the tested cells.

2.2. Battery testing schedule

Based on the established test bench shown in Fig. 2 (a), a detailed test procedure is presented in Fig. 2 (b). Three main steps are included in the test procedure: capacity calibration, EIS measurement, and aging test. The capacity calibration adopts a 0.5C (1.375 A) CC-CV charging, in which the cut-off current is 55 mA, and a 1C (2.75 A) CC discharging. The capacity calibration is performed at 25 °C, and a 1.5-hour rest period is set between the charging and discharging processes. The measured capacity is used to calculate reference battery SOH, which is defined as the ratio of residual battery capacity to the nominal capacity [45]. The EIS measurement adopts the galvanostatic mode, and the root-mean-square value of the perturbing current is 500 mA, which was determined through pre-experiments with different perturbing currents and the Kramers-Kronig transform test. The frequency range of the sweeping sines is from 0.01 Hz to 10 kHz. In our previous study [34], a wider SOC and temperature range was set in EIS measurement for battery life prediction. The emphasis of this study is to compare the performance of different EIS in battery SOH estimation; hence only one condition (the EIS at 25 °C and 50%) is taken into account.

Four cells, labeled as Cell 1 ~ 4, were considered in the aging test, in which two temperatures (25 °C and 35 °C) were involved. Different from existing cycling aging tests, this study also investigated the capacity fading and estimation performance of cells under dynamic condition aging tests. The detailed aging experiment configuration is shown in Table 1. Cell 1 and Cell 3 employed the traditional cycling aging pattern, in which the cell is charged to 4.2 V with 0.5C, followed by a 1C CC discharging, as shown in Fig. 2 (c). For these two cells, the EIS measurement was performed every 25 discharging cycles. The other two cells, Cell 2 and Cell 4, employed the new European driving cycle (NEDC) during discharging, and the maximum current rate of NEDC condition is 2C (5.5 A). The detailed aging test profile is shown in Fig. 2 (d). After a CC charging, the tested cell will go through 13 NEDC cycles until the cell voltage reaches 2.5 V. The EIS measurement and capacity calibration were performed every eight charging cycles (about 100 NEDC cycles).

2.3. Battery dataset

Following the above testing procedures, the obtained battery

Table 1
Battery aging experiment configuration.

Cell No.	Temperature	Charging	Discharging
Cell 1	25 °C	0.5C CC	1C CC
Cell 2	25 °C		NEDC
Cell 3	35 °C		1C CC
Cell 4	35 °C		NEDC

capacity and corresponding EIS during aging are shown in Fig. 3. From Fig. 3 (a) and (b), it can be found that the cells under the CC discharging show different degradation rates from those under NEDC discharging. It has been confirmed that current gradients in dynamic discharging conditions influence battery degradation [46]. From the general trend, Cell 3 at a higher cyclic temperature shows a little faster fading rate than Cell 1, as well as the condition between Cell 2 and Cell 4, which has similar characteristics to the experimental results in Ref. [47]. More experiments at a wider range of temperatures are necessary to investigate the influence of temperatures on battery aging in the future study. For the measured battery EIS, it can be confirmed that all the impedance spectra show a right-shift in the direction of the real part, meaning that the battery ohmic resistance gradually increases with the battery aging. In terms of the EIS shape, the two arcs of impedance spectrum in the mid-high frequency range are becoming more and more pronounced with the battery aging. In particular, the second arc turns larger with battery aging. Overall, 146 impedance spectra of this 18650-type battery are collected at different aging statuses, which will be utilized in the following model training and verification.

3. Methodologies

This section first exhibits fundamental techniques of the battery health estimation based on three kinds of EIS features, especially the battery ECM for impedance spectrum and the GPR-based data-driven model. Then quantitative metrics for evaluating the corresponding estimation performances are also described.

3.1. Battery EIS and impedance model

Fig. 4 (a) shows the diagram of battery EIS. Over the entire frequency range, the battery impedance spectrum can be divided into four sections: super-high, high, middle, and low-frequency sections, as presented with different colors in the impedance spectrum, which are closely related to the internal reactions of the battery. A detailed description of the impedance spectrum can be found in Refs. [26,34].

As is aforementioned, the second kind of battery feature extracted from EIS is the model parameters, and the battery model is established through the analysis of the battery impedance spectrum. Fig. 4 also shows the adopted fractional-order ECM in this study. Specifically, the impedance spectrum in the super-high frequency section can be described by an inductor L , and in particular, the intersection of the impedance spectrum and real axis corresponds to the conduction process and can be represented by a resistor R_0 . As the frequency decreases, the impedance spectrum demonstrates two arcs related to battery SEI film (high-frequency section) and the charge transfer process (middle-frequency section) [48]. Notably, one arc can be represented by a resistor and a CPE [49]. The impedance of the CPE at frequency f is detailed as follows, where Q and α ($0 \leq \alpha \leq 1$) represent the impedance coefficient and order.

$$Z_{CPE}(f) = \frac{1}{Q(j \cdot 2\pi f)^\alpha} \quad (1)$$

Finally, in the low-frequency section, the impedance spectrum appears as a straight line related to battery diffusion and can be described by a Warburg element. In this study, the Warburg element is referred to another CPE for simplicity [50], and the coefficient and order of this Warburg element are noted as W and β ($0 \leq \beta \leq 1$). Therefore, the overall impedance of the adopted battery model can be expressed as in Eq. (2).

$$Z_{model}(f) = (j \cdot 2\pi f)L + R_0 + \frac{R_1}{R_1 Q_1 (j \cdot 2\pi f)^{\alpha_1} + 1} + \frac{R_2}{R_2 Q_2 (j \cdot 2\pi f)^{\alpha_2} + 1} + \frac{1}{W(j \cdot 2\pi f)^\beta} \quad (2)$$

where R_1 , Q_1 and α_1 are corresponding to SEI film process, R_2 , Q_2 and α_2

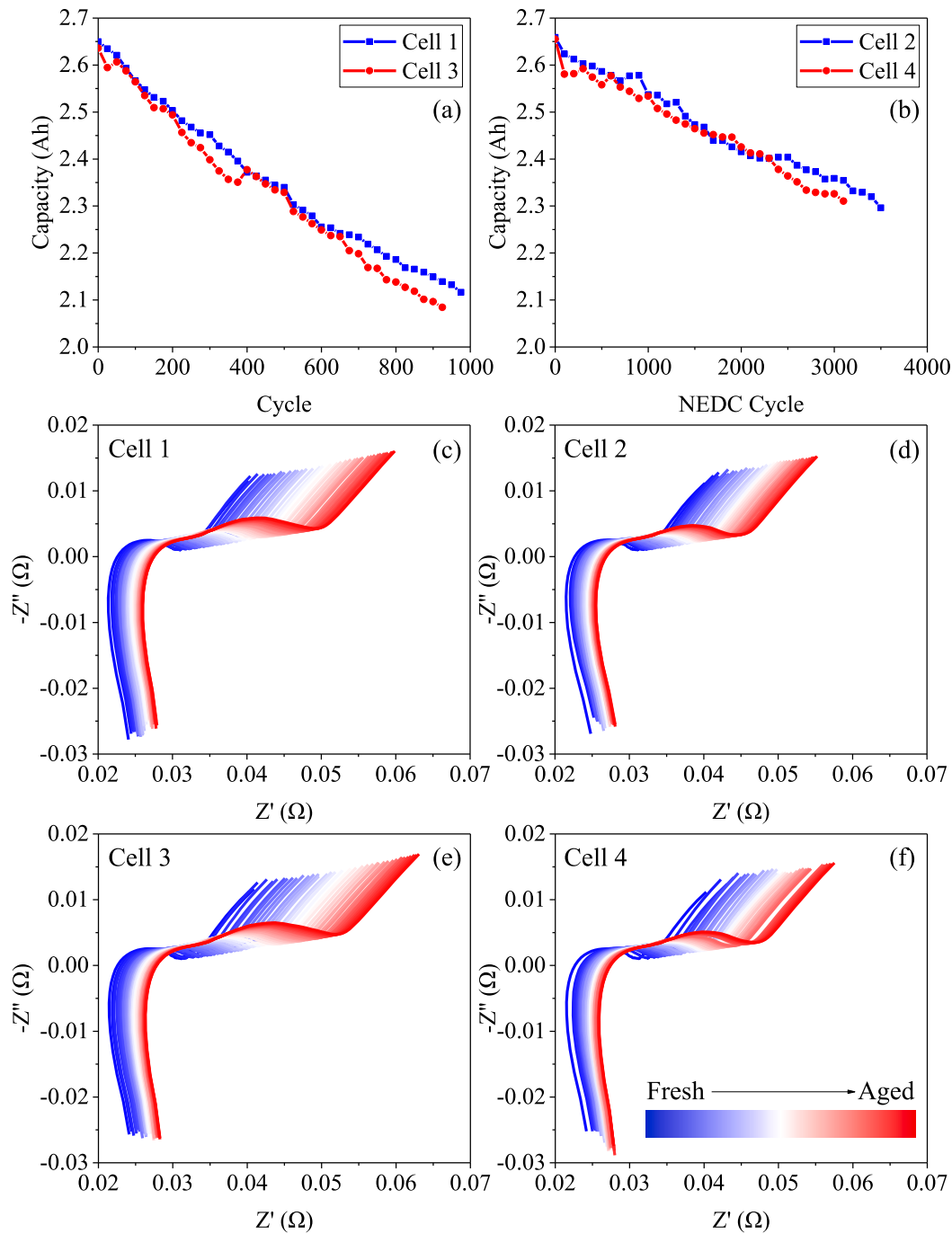


Fig. 3. Battery capacity degradation and corresponding EIS: (a) ~ (b) are capacity fading of Cell 1 ~ 4 during aging; (c) ~ (f) are the measured EIS of Cell 1 ~ 4 during aging.

are corresponding to charge transfer process.

By minimizing the difference between the calculated impedance based on Eq. (2) and the measured impedance, battery model parameters can be optimized. In this study, there are ten unknown model parameters, and the model identification is achieved by the impedance analysis software *RelaxIS* (rhd instruments GmbH & Co. KG). Based on the model identification, an impedance fitting example of Cell 1 is shown in Fig. 4 (b). It can be confirmed that the EIS fitting is very close to the original EIS data, except in the super-high frequency section. Moreover, the whole impedance spectrum is deconvoluted into several individual parts, as the underlying semicircles and a straight line in Fig. 4 (b), which can describe the battery SEI film ($R_1//CPE_1$), charge

transfer ($R_2//CPE_2$) and diffusion processes (W).

Some parameter identification results are shown in Fig. 5, including resistance R_0 , R_1 , and R_2 . From Fig. 5, it can be found that both these three resistors have a strong relationship with battery capacity and show an increasing trend with battery capacity fading. Particularly, R_2 has a maximum increasing rate among these three resistances. This phenomenon is consistent with the experimental results in Ref. [51], in which the active cathode loss and loss of lithium inventory are the dominating battery degradation factors [10]. The loss of lithium inventory reduces the lithium-ion concentration, leading to a decrease in chemical reaction rate, making the charge transfer process more difficult [41].

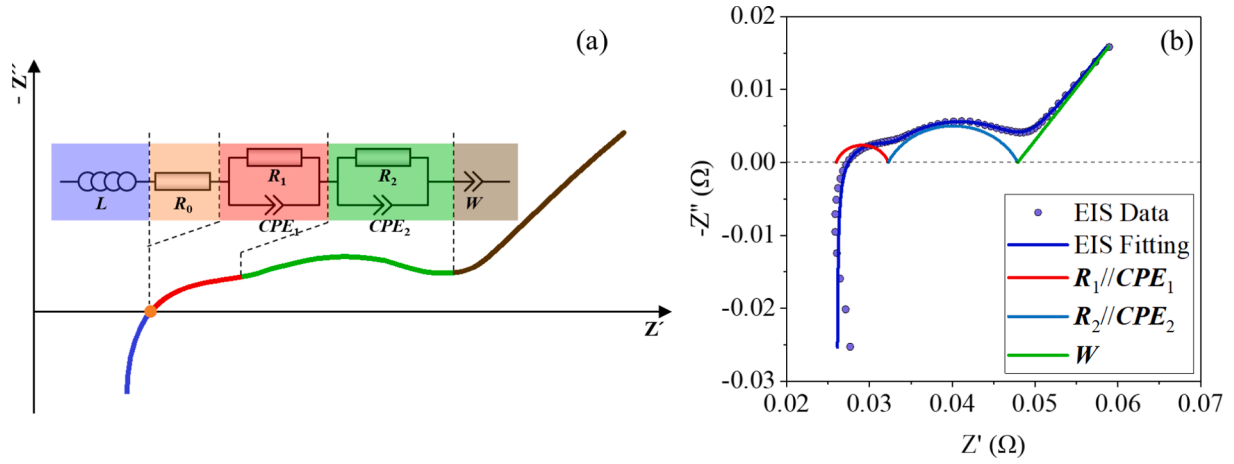


Fig. 4. The impedance modeling for battery EIS: (a) Battery fractional-order ECM; (b) The EIS fitting example.

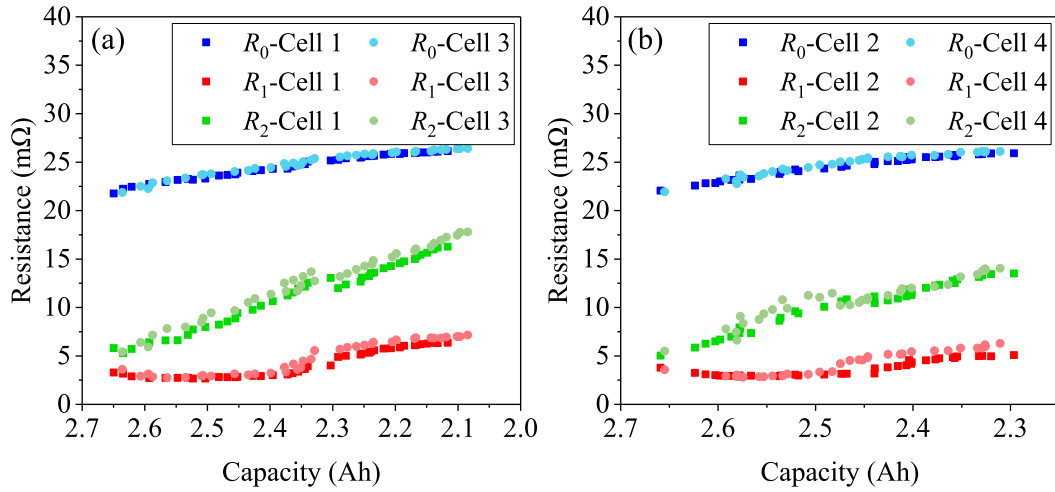


Fig. 5. The relationship between battery capacity and resistance during aging: (a) Cell 1 and Cell 3; (b) Cell 2 and Cell 4.

3.2. The regression model for SOH estimation

This study aims to comprehensively compare the performance of different EIS features in battery health estimation, so an effective machine-learning method is necessary. The GPR is a powerful technique and has been widely employed in battery SOH estimation [13,14] and life prediction [33,52]. The following introduces the adopted GPR method for regression of battery SOH.

The fundamental of GPR is based on the Gaussian process, which can be considered as a collection of random variables following the Gaussian distribution [14]. For a real system process $f(x)$, it is assumed that the probability distribution over this system satisfies the Gaussian distribution $f(x) \sim \text{gp}(m(x), k(x, x'))$, in which $m(x)$ and $k(x, x')$ are the mean and covariance functions, respectively, and are defined as follows:

$$\begin{cases} m(x) = E(f(x)) \\ k(x, x') = E[(m(x) - f(x))(m(x') - f(x')))] \end{cases} \quad (3)$$

A basic GPR model commonly adopts a zero mean function and parameterized kernel function as the covariance function, describing the similarity between two points. To enhance the performance of the GPR model, the Matern 3/2 kernel function was adopted in this study, which is more suitable for some physical processes [52]. The Matern 3/2 kernel is expressed as:

$$k(x_i, x_j | \theta) = \sigma_f^2 \left(1 + \frac{\sqrt{3}r}{\sigma_l}\right) \exp\left(-\frac{\sqrt{3}r}{\sigma_l}\right) \quad (4)$$

where σ_f is the standard deviation, σ_l is characteristic length scale. $r = \sqrt{(x_i - x_j)^T (x_i - x_j)}$ is the Euclidean distance between x_i and x_j .

For a known training set $D = (X, y) = \{(x_i, y_i) | i = 1, \dots, L\}$ (L is the length of training data, and the dimension of x_i is d), the regression between X and y can be expressed as $y = f(X) + \varepsilon$, in which ε is a Gaussian noise and satisfies $\varepsilon \sim \mathcal{N}(0, \sigma_n^2)$. Hence, the prior distribution of observed output y can be denoted as:

$$y \sim \mathcal{N}(0, K(X, X) + \sigma_n^2 \mathbf{I}) \quad (5)$$

where $K(X, X)$ is a N -dimensional symmetric positive definite matrix calculated based on Eq. (4). Based on the above derivations, the unknown parameters, which are also recognized as the GPR hyperparameters $\theta = [\sigma_f, \sigma_l, \sigma_n]$, can be optimized through minimizing the negative log marginal likelihood method [14] as follows, and the parameter optimization adopts a gradient-based method.

$$\begin{aligned} L(\theta) &= -\log p(y | \theta) \\ &= \frac{1}{2} y^T [K(X, X) + \sigma_n^2 \mathbf{I}]^{-1} y + \frac{1}{2} \log(\det(K(X, X) + \sigma_n^2 \mathbf{I})) + \frac{L}{2} \log 2\pi \end{aligned} \quad (6)$$

The above describes the modeling and optimization techniques of the GPR model. Thus, given a new data input \mathbf{x}^* which shares the identical Gaussian distribution with the training set \mathbf{X} , the joint prior distribution of observed output \mathbf{y} and predicted output \mathbf{y}^* is denoted as [53]:

$$\begin{bmatrix} \mathbf{y} \\ \mathbf{y}^* \end{bmatrix} \sim \mathcal{N} \left(0, \begin{bmatrix} K(\mathbf{X}, \mathbf{X}) + \sigma_n^2 \mathbf{I} & K(\mathbf{X}, \mathbf{x}^*) \\ K(\mathbf{X}, \mathbf{x}^*)^T & K(\mathbf{x}^*, \mathbf{x}^*) \end{bmatrix} \right) \quad (7)$$

Hence, based on Eq. (7), the predicted output \mathbf{y}^* can be further derived by calculating the posteriori distribution $p(\mathbf{y}^* | \mathbf{x}^*, \mathbf{X}, \mathbf{y})$, as shown in the following. It should be noted that $\sigma^2(\mathbf{y}^*)$ is the estimated variance. Here, the 95% confidence interval (CI) is further employed to describe the uncertainty of the GPR model. The realization of the GPR model in this study is based on Gaussian processes for machine learning toolbox [54].

$$\begin{cases} \hat{\mathbf{y}}^* = K(\mathbf{X}, \mathbf{x}^*)^T [K(\mathbf{X}, \mathbf{X}) + \sigma_n^2 \mathbf{I}]^{-1} \mathbf{y} \\ \sigma^2(\hat{\mathbf{y}}^*) = K(\mathbf{x}^*, \mathbf{x}^*) - K(\mathbf{X}, \mathbf{x}^*)^T [K(\mathbf{X}, \mathbf{X}) + \sigma_n^2 \mathbf{I}]^{-1} K(\mathbf{X}, \mathbf{x}^*) \end{cases} \quad (8)$$

$$95\% \text{ CI} = \hat{\mathbf{y}}^* \pm 1.96 \times \sigma(\hat{\mathbf{y}}^*) \quad (9)$$

3.3. EIS feature determination

Three kinds of battery EIS features are investigated in this study, including features extracted from broadband EIS, model parameters, and fixed-frequency impedance. This subsection will elaborate on the construction of the battery EIS feature for the data-driven model.

(1) Feature extracted from broadband EIS.

In the estimation approach proposed by Zhang et al. [33], the whole battery impedance spectrum data are considered as the input of the data-driven model. However, this approach has not been validated based on the EIS data from a commercial traction battery. Therefore, this study applies this feature to the SOH estimation of a commercial lithium-ion battery, and further compares it with other feature extraction methods. There are 61 different frequencies from 0.01 Hz to 10 kHz in our study; hence the dimension of $\mathbf{x}^{\text{Broadband}}$ in Eq. (10) is 122 (including the real and imaginary parts).

$$\mathbf{x}^{\text{Broadband}} = [Z_{\text{re}}(\omega_1), Z_{\text{re}}(\omega_2), \dots, Z_{\text{re}}(\omega_{61}), Z_{\text{im}}(\omega_1), Z_{\text{im}}(\omega_2), \dots, Z_{\text{im}}(\omega_{61})]^T \quad (10)$$

(2) Feature extracted from model parameters.

For the feature extracted from model parameters, an intuitive attempt is taking all the model parameters (ten parameters) into account involved in training, which is noted as $\mathbf{x}^{\text{ECM } 1}$ in Eq. (11). One consideration is that not all parameters are correlated to battery capacity fading; hence, we performed a correlation analysis between battery capacity and model parameters and found that battery resistance and impedance coefficient of CPE have a great correlation to battery capacity fading. Therefore, we construct the second feature extracted from model parameters, noted as $\mathbf{x}^{\text{ECM } 2}$. Lastly, it is reported that battery health can also be defined from the aspect of battery resistance; hence, the third feature based only on battery resistance is characterized as $\mathbf{x}^{\text{ECM } 3}$ in Eq. (11).

$$\begin{cases} \mathbf{x}^{\text{ECM } 1} = [L, R_0, R_1, Q_1, \alpha_1, R_2, Q_2, \alpha_2, W, \beta]^T \\ \mathbf{x}^{\text{ECM } 2} = [R_0, R_1, Q_1, R_2, Q_2]^T \\ \mathbf{x}^{\text{ECM } 3} = [R_0, R_1, R_2]^T \end{cases} \quad (11)$$

(3) Feature extracted from fixed-frequency impedance.

The above two feature determination methods require the knowl-

edge of broadband EIS. Nevertheless, broadband measurement is time-consuming or unavailable. Therefore, the measurement of a fixed-frequency impedance is more practical and accessible. For the determination of measurement frequency, the automatic relevance determination has been employed in the selection of EIS frequency [33]. The problem is that this kind of method may obtain a super-high/low frequency, which is still challenging to achieve. Other research attempted to use a defined frequency to identify battery life, in which the defined frequency is determined through the investigation of EIS trends during battery aging [55]. Therefore, in our study, the third EIS feature adopts the defined frequencies determined from experience. As shown in Fig. 5, R_2 in the middle-frequency section has the most noticeable change during battery aging, whereas the middle-frequency section is mainly within $10^{-1} \sim 10^2$. Hence, considering the actual sampling ability, the battery impedance at 1 Hz, 5 Hz (5.0119 Hz in this study), and 10 Hz, and their combinations, are utilized in constructed features, as shown in Eq. (12). It has been confirmed that the Pearson correlation coefficients ($|\rho|$) between capacity fading and the real and imaginary parts of battery impedance at these three frequencies are larger than 0.95.

$$\begin{cases} \mathbf{x}^{\text{Fixed } 1} = [Z_{\text{re}}(1), Z_{\text{im}}(1)]^T \\ \mathbf{x}^{\text{Fixed } 2} = [Z_{\text{re}}(5), Z_{\text{im}}(5)]^T \\ \mathbf{x}^{\text{Fixed } 3} = [Z_{\text{re}}(10), Z_{\text{im}}(10)]^T \\ \mathbf{x}^{\text{Fixed } 4} = [Z_{\text{re}}(1), Z_{\text{re}}(5), Z_{\text{im}}(1), Z_{\text{im}}(5)]^T \\ \mathbf{x}^{\text{Fixed } 5} = [Z_{\text{re}}(1), Z_{\text{re}}(10), Z_{\text{im}}(1), Z_{\text{im}}(10)]^T \\ \mathbf{x}^{\text{Fixed } 6} = [Z_{\text{re}}(5), Z_{\text{re}}(10), Z_{\text{im}}(5), Z_{\text{im}}(10)]^T \\ \mathbf{x}^{\text{Fixed } 7} = [Z_{\text{re}}(1), Z_{\text{re}}(5), Z_{\text{re}}(10), Z_{\text{im}}(1), Z_{\text{im}}(5), Z_{\text{im}}(10)]^T \end{cases} \quad (12)$$

3.4. Performance metrics

To quantitatively compare the performance of health estimation with different EIS features, three accuracy metrics are employed in this study, including the maximum absolute error (MaxAE), mean absolute error (MAE), and root-mean-square error (RMSE), as defined in the following:

$$\begin{cases} \text{MaxAE} = \max(|y_i - \hat{y}_i|) \\ \text{MAE} = \frac{1}{N} \sum_{i=1}^N |y_i - \hat{y}_i| \\ \text{RMSE} = \sqrt{\frac{1}{N} \sum_{i=1}^N (y_i - \hat{y}_i)^2} \end{cases} \quad (13)$$

where y_i and \hat{y}_i are the real and estimated values. Specifically, the MaxAE is more sensitive to the outliers, while the MAE and RMSE are the errors in the average sense.

The confidence metrics are derived from Eqs. (8) and (9), including the coverage probability (CP) [56] and mean standard deviation (MSD) [57], as shown in follows:

$$\begin{cases} \text{CP} = \frac{\gamma_{95\%}}{N} \times 100\% \\ \text{MSD} = \frac{1}{N} \sum_{i=1}^N \sigma(\hat{y}_i) \end{cases} \quad (14)$$

where $\gamma_{95\%}$ means the number of actual SOH in the estimated 95% CI, and a 100% CP means that the estimated CI can cover all the actual values. However, the problem is that if the estimated variance is large, it is easy to reach the ideal coverage. Therefore, the MSD is employed simultaneously, which means the average of the standard deviation, and a small MSD represents small uncertainties.

Except for the above accuracy and confidence metrics, the computational burden is also considered in this study, including the training time and test time. All the estimation training and test are carried out on a personal computer, with the processor of Intel i7-8550 and the environment of MATLAB R2020a. To reduce the interference caused by the

computational operation's randomness, the final computational time is the average of ten runs' time cost. It should be noted that the computational burden here does not take the ECM parameter identification into account. To verify the performance of each feature comprehensively, the multiple-test is employed, as shown in Fig. 6.

Specifically, for one kind of EIS feature, the estimation will run four times, and at each time, a different cell will be considered as the test cell, and the remaining cells are considered as training cells. The model output is battery SOH, while the model input is the EIS feature.

4. Comparative analysis of battery SOH estimation

As mentioned above, the health features based on broadband EIS, model parameters, and fixed-frequency impedance are considered as the typical data-driven features, further employed in the comparative analysis in this study. This section examines the performance of each EIS feature quantitatively, together with the GPR model as the basic data-driven technique. Particularly, estimation accuracy, certainty, and efficiency are the main comparative metrics.

4.1. Estimation study 1: Using feature extracted from broadband EIS

The performance of SOH estimation using features based on broadband EIS $x^{\text{Broadband}}$ is illustrated in Fig. 7. Based on the schedule of the multiple-test, four training and test cases are performed, and then estimation results of four cells are obtained. It can be confirmed that the SOH estimation results both show good agreement with the reference values during the whole life-cycle for these four cells with different aging patterns. The estimated values of Cell 4 at 1750 to 2250 cycles deviate much from the reference SOH in Fig. 7 (d). The estimation deviation in the data-driven method may come from the different characteristics between training and test data. Nevertheless, the SOH MaxAE is still within 3% in this case, which is superior to some existing data-driven estimation methods using the battery voltage and temperature as the data features [58]. Usually, a MaxAE within 5% is acceptable [59]. Except for the estimated values, the 95% CIs are also presented in the figure. As presented in Fig. 7 (a) and (b), the 95% CIs maintain a relatively stable estimation uncertainty, reflecting the effectiveness of the employed broadband EIS as the data-driven feature. However, for the results of Cell 3 and Cell 4 in Fig. 7 (c) and (d), with battery aging, the estimated CIs become more considerable, meaning that battery aging aggravates the uncertainty of health estimation. Moreover, it can be found that, even though the estimation of Cell 4 has a large CI, there are still many reference SOHs that are not covered by the estimation interval.

Table 2 summarizes the performance indicators of four cells based on the broadband EIS. Consistent with the above figure, the SOH estimation MaxAE, MAE, and RMSE of Cell 4 are 2.809%, 1.462%, and 1.620%, respectively, showing the most significant estimation error. Cell 3 has

the optimal accuracy, with the RMSE over the life-cycle smaller than 1%. At the expense of 0.296% in MaxAE and 0.136% in RMSE, Cell 2 achieves a better confidence performance, with the CP of 75% and MSD of 0.672%. For the estimation efficiency, Cell 1 is with the least training and test time. The reason for the least training time is that this case has the minimum number of iterations. Lastly, the average of each cell's performance results is calculated as the final performance indicators of the employed features based on wide-EIS frequency.

4.2. Estimation study 2: Using feature extracted from model parameters

The next is the battery health estimation using features based on model parameters. It has been mentioned that the model parameter identification is realized through a professional software named *Relaxis*, and the identification results show that the R^2 of both impedance fitting is larger than 0.99. Among the ten obtained model parameters, R_0, R_1, R_2, Q_1 and Q_2 show a significant increasing trend with battery aging, and the Pearson correlation coefficients between these parameters and battery capacity are larger than 0.8. As presented in Eq. (11), we construct three kinds of data features based on ECM parameters, and the estimation results are shown in Fig. 8.

Among the three estimations based on different model parameters, an evident situation is found that not the higher the input dimension, the better the estimation effect. In most cycles of these four cells, the estimation using $x^{\text{ECM } 2}$ shows better accuracy than that using $x^{\text{ECM } 1}$, especially for the estimation of Cell 1 and Cell 4. This implies that the non-strongly correlated model parameters play a slightly negative role in battery health estimation. For the last feature $x^{\text{ECM } 3}$ only considering the battery resistance, the SOH estimation shows a larger deviation from the actual SOH, particularly at the fluctuation of model parameters in Fig. 5. The maximum error happens in the estimation of Cell 4, and the MaxAE is about 5.5%. The estimation uncertainties of these three features are also shown in Fig. 8. Apparently, except for estimation accuracy, the estimation uncertainties also demonstrate different characteristics. Generally, the results using $x^{\text{ECM } 2}$ show better estimation confidence for these four cells, while those using $x^{\text{ECM } 1}$ and $x^{\text{ECM } 3}$ exist the conditions of small CP and large MSD. This also proves the superior performance of feature $x^{\text{ECM } 2}$.

Furthermore, Table 3 presents the quantitative metrics of the estimation based on model parameters. For the estimation accuracy, the maximum MaxAE of these four cells using different model parameters as the data feature are 3.544%, 3.350%, and 5.413%. In terms of indicator MAE and RMSE, the estimation using feature $x^{\text{ECM } 2}$ also performs better. Besides, for different cells, the estimation based on feature $x^{\text{ECM } 2}$ provides the CP larger than 80% and the MSD in SOH smaller than 1%. For computational efficiency, there is not much difference in the training and test time of these three features. Lastly, the average of each cell's performance indicators is considered as the final performance of the employed data feature. It can be found that feature $x^{\text{ECM } 2}$ shows the best comprehensive performance.

4.3. Estimation study 3: Using feature extracted from fixed-frequency impedance

The last is the estimation based on fixed-frequency impedance, and three points in the middle-frequency section are employed to construct the data feature. For simplicity of the expression, only the estimation results using $x^{\text{Fixed } 1}, x^{\text{Fixed } 2}, x^{\text{Fixed } 3}$, and $x^{\text{Fixed } 7}$ are shown in Fig. 9.

The estimation results show that only using the battery impedance at a single frequency can still achieve acceptable estimation results. During the life-cycle of these four cells, an estimation performance with MaxAE smaller than 3.3% can be confirmed using features $x^{\text{Fixed } 1}, x^{\text{Fixed } 2}$, and $x^{\text{Fixed } 3}$. This indicator is better than the MaxAE of estimation results using model parameters. With impedance data at all three frequencies involved in training, the estimation accuracy has improved (the MaxAE

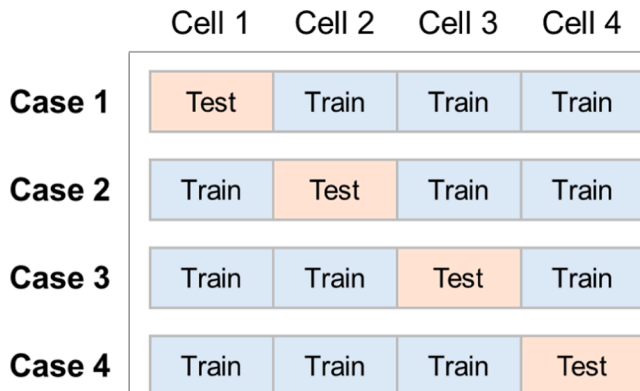


Fig. 6. The diagram of the multiple-test.

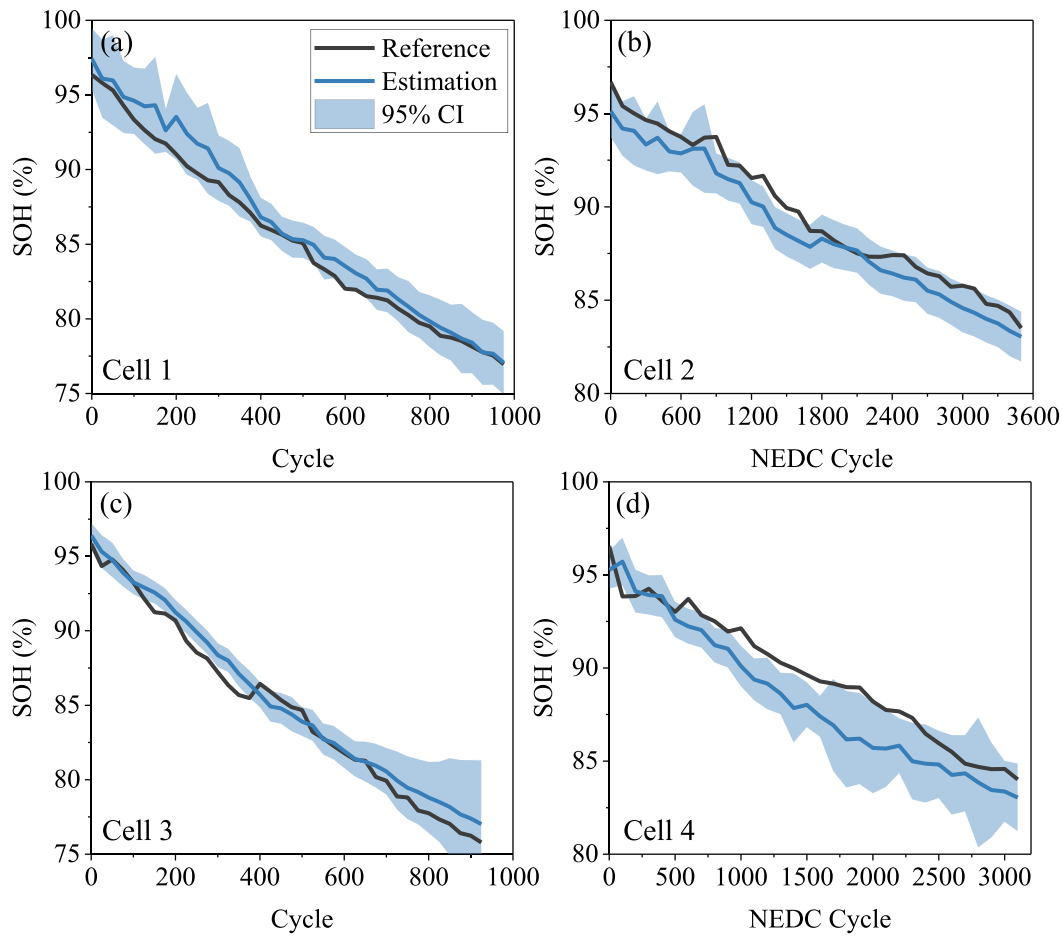


Fig. 7. Battery SOH estimation results using feature based on broadband EIS: (a) ~ (d) are estimation results of Cell 1 ~ Cell 4.

Table 2

Performance indicators for each cell using feature based on broadband EIS.

Feature	Cell No.	Accuracy			Confidence		Efficiency	
		MaxAE (%)	MAE (%)	RMSE (%)	CP (%)	MSD (%)	Training (s)	Test (s)
Broadband EIS	Cell 1	2.506	0.880	1.101	95	0.975	0.721	0.0069
	Cell 2	1.951	0.935	1.044	75	0.672	1.024	0.0087
	Cell 3	1.655	0.786	0.908	76.316	0.739	0.903	0.0074
	Cell 4	2.809	1.462	1.620	46.875	0.836	0.834	0.0093
	Average	2.230	1.016	1.168	73.298	0.806	0.870	0.0081

is smaller than 3.0%), and the estimated SOHs are further closer to the real SOHs. The reason for the high estimation accuracy lies in that the selected three frequencies are within the middle frequency section of EIS, which reflects the change in the battery charge transfer process. A close relationship between battery aging and the charge transfer process has been reported in Refs. [34,41]. Moreover, significant growth in R_2 can be found in Fig. 5. Hence, this contributes to the accurate estimation. Similar to estimation accuracy, only using battery impedance at 1 Hz or 10 Hz presents larger estimation uncertainty, while the other two data features have better confidence in battery SOH estimation.

Table 4 shows the final performance indicators of the estimation based on these fixed-frequency impedance features. Both the estimation accuracy, confidence, and efficiency show an improvement trend with more impedance data at these three frequencies involved in training. Overall, the performance difference is not obvious among these data features. Feature $x^{\text{Fixed } 7}$ provides the smallest MaxAE and least training time, feature $x^{\text{Fixed } 4}$ shows a slightly better MAE and RMSE, and feature $x^{\text{Fixed } 6}$ has the smallest MSD. It is worth highlighting that feature $x^{\text{Fixed } 7}$

with the largest dimension among the seven features has less training time. We also found that the training process using $x^{\text{Fixed } 7}$ has the least iterations before convergence. This implies that using strong-related features can speed up the training process. After overall evaluation, feature $x^{\text{Fixed } 7}$ is considered to have superior performance.

4.4. Comparisons of estimation performance

The above discusses the performance of three kinds of EIS features in SOH estimation, and $x^{\text{ECM } 2}$ and $x^{\text{Fixed } 7}$ are further considered as the superior features among the sub-kinds. To obtain the EIS feature with excellent performance, a comprehensive comparison between $x^{\text{Broadband}}$, $x^{\text{ECM } 2}$, and $x^{\text{Fixed } 7}$ is performed, as shown in Fig. 10.

It can be found that the broadband EIS feature and the fixed-frequency impedance feature have similar performance in SOH estimation MaxAE, while the latter has 0.266% and 0.236% improvement in the estimation MAE and RMSE, respectively. The fixed-frequency

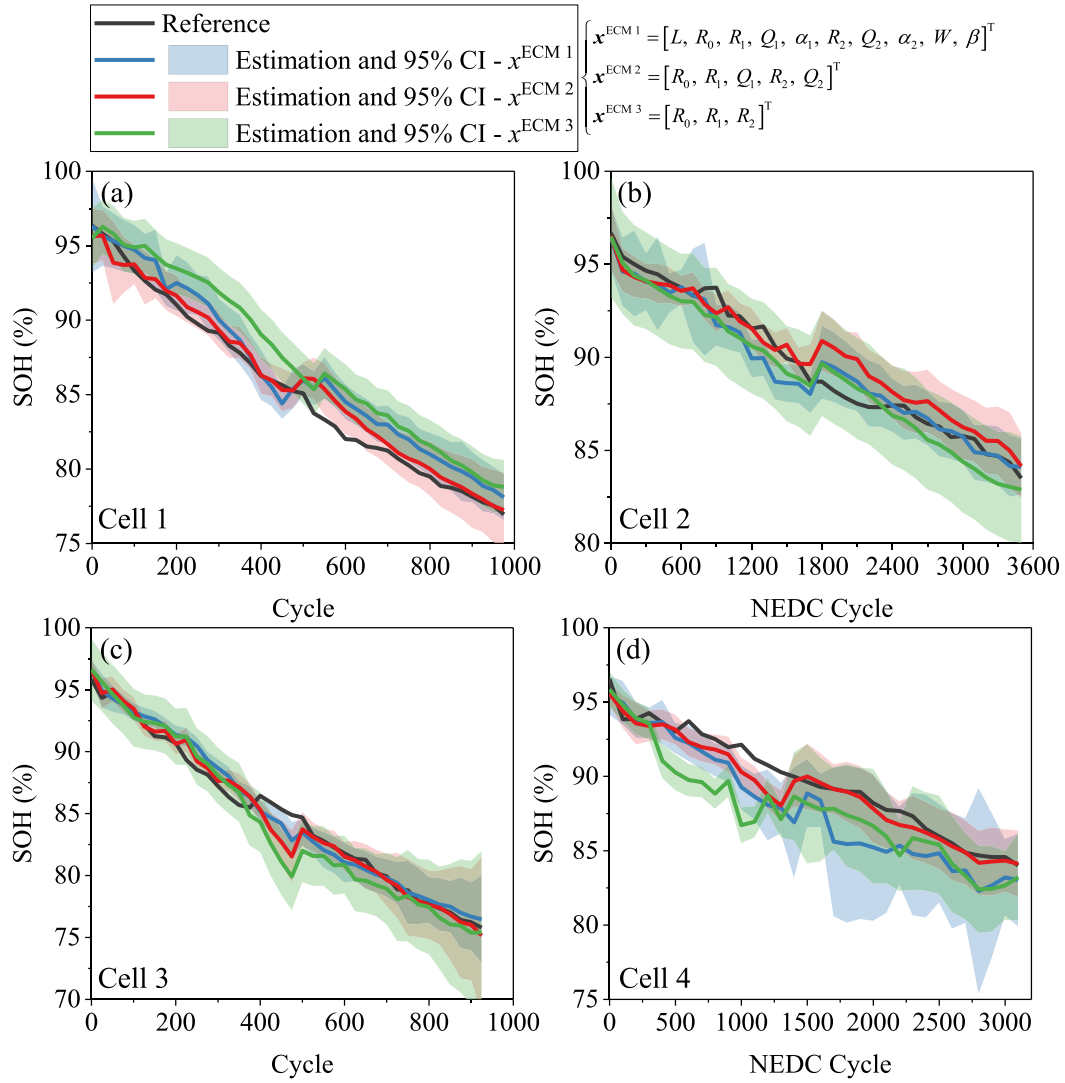


Fig. 8. Battery SOH estimation results using features based on model parameters: (a) ~ (d) are estimation results of Cell 1 ~ Cell 4.

Table 3

Performance indicators for each cell using features based on model parameters.

Feature	Cell No.	Accuracy			Confidence			Efficiency
		MaxAE (%)	MAE (%)	RMSE (%)	CP (%)	MSD (%)	Training (s)	Test (s)
ECM 1	Cell 1	2.806	1.292	1.472	57.5	0.787	0.391	0.0054
	Cell 2	2.025	0.691	0.883	83.333	0.788	0.509	0.0051
	Cell 3	2.054	0.808	0.957	65.789	0.702	0.455	0.0047
	Cell 4	3.544	1.799	2.058	81.25	1.448	0.835	0.0057
	Average	2.607	1.147	1.342	71.968	0.931	0.548	0.0052
ECM 2	Cell 1	2.304	0.652	0.863	87.5	0.805	0.475	0.0051
	Cell 2	2.385	0.827	1.040	80.556	0.671	0.416	0.0050
	Cell 3	3.350	0.628	0.975	81.579	0.904	0.528	0.0050
	Cell 4	2.243	0.617	0.851	81.25	0.817	0.381	0.0048
	Average	2.570	0.681	0.932	82.721	0.799	0.450	0.0050
ECM 3	Cell 1	3.343	2.151	2.283	30	0.878	0.417	0.0046
	Cell 2	1.607	0.858	0.939	100	1.372	0.643	0.0054
	Cell 3	4.954	1.213	1.597	89.474	1.494	0.380	0.0048
	Cell 4	5.413	2.002	2.320	65.625	1.157	0.374	0.0047
	Average	3.829	1.556	1.784	71.275	1.225	0.453	0.0049

impedance feature originates from the broadband feature; however, the high dimensional, wide frequency feature cannot provide the optimal estimation accuracy in the data-driven technique employed in this study. One reason may be that the data on other frequencies have a weak

correlation to battery capacity and affect the parameter optimization process in Eq. (6) because the GPR method uses the whole samples' information to perform the prediction. Moreover, it has been mentioned that the GPR model loses efficiency when dealing with high-dimensional

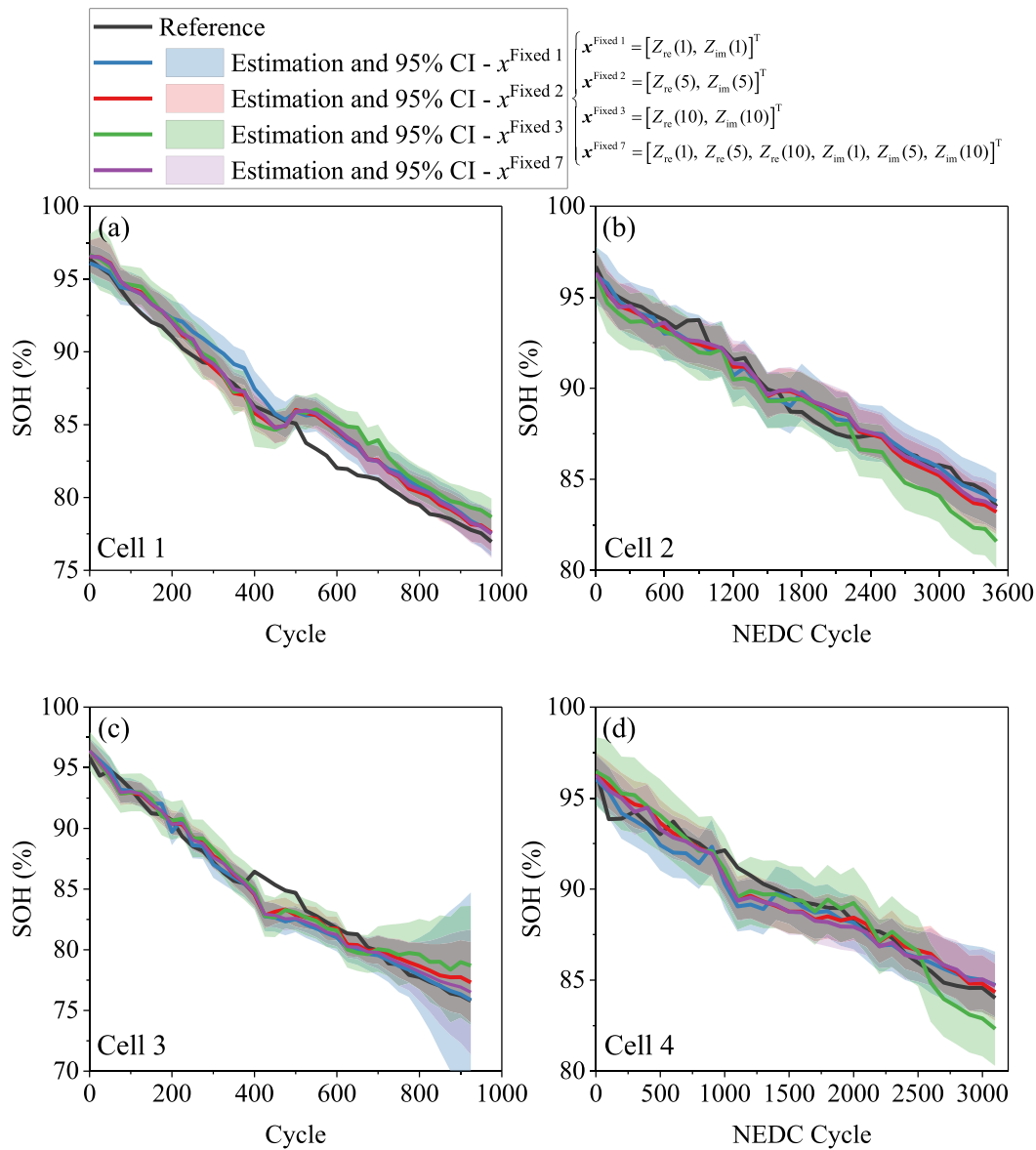


Fig. 9. Battery SOH estimation results using features based on fixed-frequency impedance: (a) ~ (d) are estimation results of Cell 1 ~ Cell 4.

Table 4

Performance indicators for each cell using features based on fixed-frequency impedance.

Feature	Accuracy			Confidence		Efficiency	
	MaxAE (%)	MAE (%)	RMSE (%)	CP (%)	MSD (%)	Training (s)	Test (s)
Fixed 1	2.251	0.767	0.967	78.298	0.796	0.540	0.0052
Fixed 2	2.228	0.765	0.926	85.013	0.634	0.503	0.0053
Fixed 3	2.745	1.096	1.300	75.929	0.868	0.688	0.0050
Fixed 4	2.246	0.725	0.907	82.225	0.670	0.515	0.0052
Fixed 5	2.361	0.788	0.988	77.628	0.727	0.492	0.0052
Fixed 6	2.249	0.790	0.971	75.397	0.624	0.618	0.0053
Fixed 7	2.194	0.750	0.932	80.888	0.660	0.454	0.0053

problems [60]. The model parameter feature has the largest MaxAE in SOH estimation, and the fluctuations during the life-cycle are apparent. One essential procedure of this estimation method is the model parameter identification, which may introduce the identification error and further influence the estimation accuracy.

For the estimation confidence in Fig. 10 (b), the model parameter feature has the most extensive estimation coverage, mainly due to the comparatively large estimation variance (reflected through the MSD

value). In comparison, the fixed-frequency impedance feature has a relatively small MSD in terms of estimation confidence, indicating the superior performance of this kind of EIS feature. At last, the computational time is presented in Fig. 10 (c). Apparently, the higher the dimension of the input features, the longer the training and test time, and the training time of the broadband feature is about 1.9 times that of the model parameter feature and fixed-frequency impedance feature. It is not much difference between the latter two kinds of EIS features. This

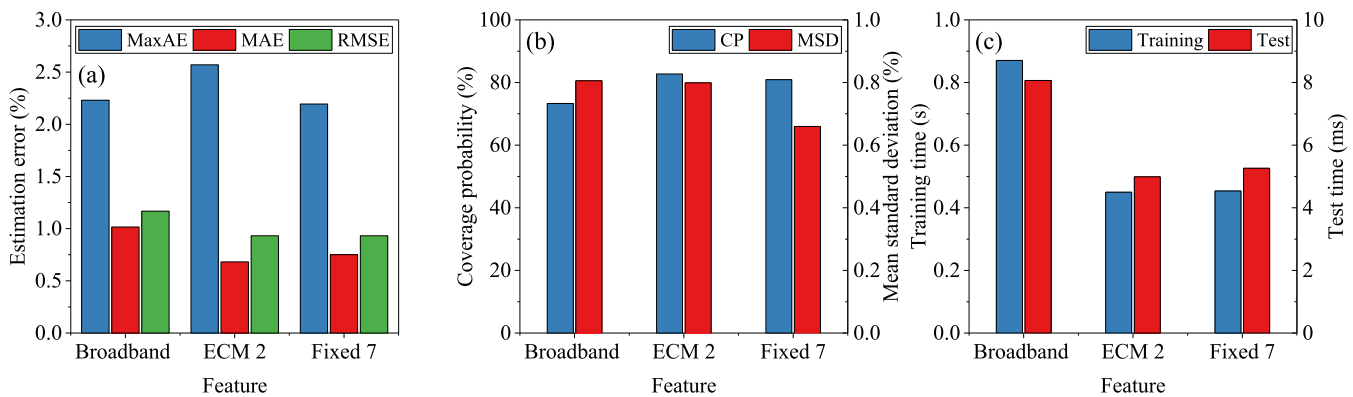


Fig. 10. The comparisons of estimation performance using different EIS features: (a) ~ (c) are the results of estimation accuracy, confidence, and efficiency.

implies that the estimation method using the fixed-frequency impedance feature is promising to be operated in a real application. Moreover, battery SOH has slow-varying characteristics [61], which means it only needs to be updated once in a few hours.

The above analysis concludes that the fixed-frequency impedance feature has comprehensively optimal performance in estimation accuracy, confidence, and efficiency, followed by the model parameter and broadband features. This will provide valuable evidence to develop suitable EIS features for battery health state estimation. Nevertheless, what is not considered in this paper is the enforceability of obtaining the EIS feature. For the three EIS features studied in this paper, the fixed-frequency impedance feature is the most accessible, comparatively, because the other two EIS features need information of the broadband impedance. Actually, the complete broadband impedance from super-high to low-frequency section is complicated and time-consuming to obtain. Moreover, up to 10 parameters are involved in the employed ECM, and accurately identifying these parameters online is still a critical problem. Some simple heuristic algorithms may not converge in the identification of model parameters. Therefore, we highlight that using the proper frequency point as the EIS feature can achieve outstanding performance in battery SOH estimation.

5. Conclusions

Battery electrochemical impedance contains much helpful information and closely relates to battery aging. This study conducts systematic comparison research of three representative EIS features in battery SOH assessment, which are broadband EIS, model parameters, and fixed-frequency impedance extracted from battery EIS. A battery EIS dataset is constructed to perform the data-driven estimation, in which the constant and dynamic discharging conditions are considered during battery cycling aging. Based on the employed GPR model, the performance of each data feature is achieved in terms of estimation accuracy, confidence, and efficiency. The experimental results show that all three data features have a strong generalization for different cells working under different aging conditions, and the maximum estimation deviation during the life-cycle is within 5.5%. The performance metrics highlight that using the proper frequency point as the data feature has comprehensively outstanding performance in battery SOH estimation. Specifically, the fixed-frequency impedance feature has a 0.38% improvement in the estimation MaxAE over the model parameter feature, has a 7.59% increase in estimation coverage, and saves about 48% of training time compared to the broadband EIS feature. This study provides valuable evidence to develop optimal EIS features for battery health state estimation.

This study comprehensively compares the performance of different EIS features in battery SOH estimation. In future research, the implementation of the proposed SOH estimation approach in a real vehicle

should be investigated. More battery EIS data covering diverse aging conditions will be helpful for the model construction, enhancing the estimation robustness. Moreover, the influence of battery SOC and temperature shall be considered during estimation; especially it has been proved that battery temperature has a significant impact on the battery impedance characteristics; hence, SOH estimation based on EIS features under battery multi-state interference will be of great significance for battery management. In this study, we conclude that the fixed-frequency impedance feature has the superior estimation only based on performance metrics; nevertheless, a more intelligent decision method considering the importance of performance metrics and application scenario will be helpful to make a more meaningful conclusion.

CRediT authorship contribution statement

Bo Jiang: Conceptualization, Methodology, Software, Data curation, Formal analysis, Validation, Writing – original draft, Writing – review & editing. **Jiangong Zhu:** Investigation, Software, Data curation, Validation, Writing – review & editing. **Xueyuan Wang:** Methodology, Software, Data curation, Validation, Writing – original draft. **Xuezhe Wei:** Supervision, Writing – review & editing. **Wenlong Shang:** Investigation, Writing – review & editing. **Haifeng Dai:** Investigation, Resources, Funding acquisition, Project administration, Writing – review & editing.

Declaration of Competing Interest

The authors declare that they have no known competing financial interests or personal relationships that could have appeared to influence the work reported in this paper.

Data availability

Data will be made available on request.

Acknowledgment

This work is financially supported by the National Natural Science Foundation of China (NSFC, Grant No. U20A20310, 52107230).

References

- [1] Zhu J, Knapp M, Sørensen DR, Heere M, Darma MSD, Müller M, et al. Investigation of capacity fade for 18650-type lithium-ion batteries cycled in different state of charge (SoC) ranges. *J Power Sources* 2021;489:229422. <https://doi.org/10.1016/j.jpowsour.2020.229422>.
- [2] Jiang B, Dai H, Wei X, Jiang Z. Multi-kernel relevance vector machine with parameter optimization for cycling aging prediction of lithium-ion batteries. *IEEE journal of emerging and selected topics in power. Electronics* 2021:1–12.
- [3] Qiao D, Wang X, Lai X, Zheng Y, Wei X, Dai H. Online quantitative diagnosis of internal short circuit for lithium-ion batteries using incremental capacity method. *Energy* 2022;243:123082. <https://doi.org/10.1016/j.energy.2021.123082>.

- [4] Xiong R, Pan Y, Shen W, Li H, Sun F. Lithium-ion battery aging mechanisms and diagnosis method for automotive applications: Recent advances and perspectives. *Renew Sustainable Energy Rev* 2020;131:110048. <https://doi.org/10.1016/j.rser.2020.110048>.
- [5] Dai H, Jiang Bo, Hu X, Lin X, Wei X, Pecht M. Advanced battery management strategies for a sustainable energy future: multilayer design concepts and research trends. *Renew. Sustainable Energy Rev* 2021;138:110480. <https://doi.org/10.1016/j.rser.2020.110480>.
- [6] Li Y, Stroe D-I, Cheng Y, Sheng H, Sui X, Teodorescu R. On the feature selection for battery state of health estimation based on charging–discharging profiles. *J Energy Storage* 2021;33:102122. <https://doi.org/10.1016/j.est.2020.102122>.
- [7] Wang Y, Tian J, Sun Z, Wang Li, Xu R, Li M, et al. A comprehensive review of battery modeling and state estimation approaches for advanced battery management systems. *Renew. Sustainable Energy Rev* 2020;131:110015. <https://doi.org/10.1016/j.rser.2020.110015>.
- [8] Santhanagopalan S, Zhang Qi, Kumaresan K, White RE. Parameter estimation and life modeling of lithium-ion cells. *J Electrochem Soc* 2008;155(4):A345. <https://doi.org/10.1149/1.2839630>.
- [9] Xiong R, Li L, Li Z, Yu Q, Mu H. An electrochemical model based degradation state identification method of Lithium-ion battery for all-climate electric vehicles application. *Appl Energy* 2018;219:264–75.
- [10] Bi Y, Yin Y, Choe S-Y. Online state of health and aging parameter estimation using a physics-based life model with a particle filter. *J Power Sources* 2020;476:228655. <https://doi.org/10.1016/j.jpowsour.2020.228655>.
- [11] Jiang Bo, Dai H, Wei X, Xu T. Joint estimation of lithium-ion battery state of charge and capacity within an adaptive variable multi-timescale framework considering current measurement offset. *Appl Energy* 2019;253:113619. <https://doi.org/10.1016/j.apenergy.2019.113619>.
- [12] Yang D, Wang Y, Pan R, Chen R, Chen Z. State-of-health estimation for the lithium-ion battery based on support vector regression. *Appl Energy* 2018;227:273–83.
- [13] Li X, Yuan C, Wang Z. Multi-time-scale framework for prognostic health condition of lithium battery using modified Gaussian process regression and nonlinear regression. *J Power Sources* 2020;467:228358. <https://doi.org/10.1016/j.jpowsour.2020.228358>.
- [14] Yang D, Zhang Xu, Pan R, Wang Y, Chen Z. A novel Gaussian process regression model for state-of-health estimation of lithium-ion battery using charging curve. *J Power Sources* 2018;384:387–95.
- [15] Li Yi, Zou C, Berecibar M, Nanini-Maury E, Chan J-W, van den Bossche P, et al. Random forest regression for online capacity estimation of lithium-ion batteries. *Appl Energy* 2018;232:197–210.
- [16] Liu K, Peng Q, Sun H, Fei M, Ma H, Hu T. A transferred recurrent neural network for battery calendar health prognostics of energy-transportation systems. *IEEE Trans Ind Inf* 2022;1–10.
- [17] Li W, Sengupta N, Dechent P, Howey D, Annaswamy A, Sauer DU. Online capacity estimation of lithium-ion batteries with deep long short-term memory networks. *J Power Sources* 2021;482:228863. <https://doi.org/10.1016/j.jpowsour.2020.228863>.
- [18] Fan Y, Xiao F, Li C, Yang G, Tang X. A novel deep learning framework for state of health estimation of Lithium-ion battery. *J Energy Storage* 2020;32:101741. <https://doi.org/10.1016/j.est.2020.101741>.
- [19] Hu C, Jain G, Zhang P, Schmidt K, Gomadam P, Gorka T. Data-driven method based on particle swarm optimization and k-nearest neighbor regression for estimating capacity of lithium-ion battery. *Appl Energy* 2014;129:49–55.
- [20] Lu C, Tao L, Fan H. Li-ion battery capacity estimation: a geometrical approach. *J Power Sources* 2014;261:141–7.
- [21] Shen S, Sadoughi M, Chen X, Hong M, Hu C. A deep learning method for online capacity estimation of lithium-ion batteries. *J Energy Storage* 2019;25:100817. <https://doi.org/10.1016/j.est.2019.100817>.
- [22] Li Y, Li K, Liu X, Wang Y, Zhang Li. Lithium-ion battery capacity estimation — a pruned convolutional neural network approach assisted with transfer learning. *Appl Energy* 2021;285:116410. <https://doi.org/10.1016/j.apenergy.2020.116410>.
- [23] Bertinelli Salucci C, Bakdi A, Glad IK, Vanem E, De Bin R. Multivariable fractional polynomials for lithium-ion batteries degradation models under dynamic conditions. *J Energy Storage* 2022;52:104903. <https://doi.org/10.1016/j.est.2022.104903>.
- [24] Zhang Y, Wik T, Bergström J, Pecht M, Zou C. A machine learning-based framework for online prediction of battery ageing trajectory and lifetime using histogram data. *J Power Sources* 2022;526:231110. <https://doi.org/10.1016/j.jpowsour.2022.231110>.
- [25] Deng Z, Hu X, Lin X, Xu Le, Che Y, Hu L. General discharge voltage information enabled health evaluation for lithium-ion batteries. *IEEE/ASME Trans Mechatron* 2021;26(3):1295–306.
- [26] Wang X, Wei X, Zhu J, Dai H, Zheng Y, Xu X, et al. A review of modeling, acquisition, and application of lithium-ion battery impedance for onboard battery management. *eTransportation* 2021;7:100093. <https://doi.org/10.1016/j.etrans.2020.100093>.
- [27] Yin Y, Hu Y, Choe S-Y, Cho H, Joe WT. New fast charging method of lithium-ion batteries based on a reduced order electrochemical model considering side reaction. *J Power Sources* 2019;423:367–79.
- [28] Wang X, Wei X, Chen Q, Dai H. A novel system for measuring alternating current impedance spectra of series-connected lithium-ion batteries with a high-power dual active bridge converter and distributed sampling units. *IEEE Trans Ind Electron* 2021;68(8):7380–90.
- [29] Koseoglou M, Tsioumas E, Papagiannis D, Jabbour N, Mademlis C. A novel on-board electrochemical impedance spectroscopy system for real-time battery impedance estimation. *IEEE Trans Power Electron* 2021;36(9):10776–87.
- [30] Westerhoff U, Kroker T, Kurbach K, Kurrat M. Electrochemical impedance spectroscopy based estimation of the state of charge of lithium-ion batteries. *J Energy Storage* 2016;8:244–56.
- [31] Zhu JG, Sun ZC, Wei XZ, Dai HF. A new lithium-ion battery internal temperature on-line estimate method based on electrochemical impedance spectroscopy measurement. *J Power Sources* 2015;274:990–1004.
- [32] Wang X, Wei X, Chen Q, Zhu J, Dai H. Lithium-ion battery temperature on-line estimation based on fast impedance calculation. *J Energy Storage* 2019;26:100952. <https://doi.org/10.1016/j.est.2019.100952>.
- [33] Zhang Y, Tang Q, Zhang Y, Wang J, Stimming U, Lee AA. Identifying degradation patterns of lithium ion batteries from impedance spectroscopy using machine learning. *Nat Commun* 2020;11:1706.
- [34] Wang X, Li R, Dai H, Zhang N, Chen Q, Wei X. A novel dual time scale life prediction method for lithium-ion batteries considering effects of temperature and state of charge. *Int J Energy Res* 2021;14692–14709.
- [35] Pastor-Fernández C, Uddin K, Chouchelamane GH, Widanage WD, Marco J. A comparison between electrochemical impedance spectroscopy and incremental capacity-differential voltage as li-ion diagnostic techniques to identify and quantify the effects of degradation modes within battery management systems. *J Power Sources* 2017;360:301–18.
- [36] Koseoglou M, Tsioumas E, Ferentinou D, Jabbour N, Papagiannis D, Mademlis C. Lithium plating detection using dynamic electrochemical impedance spectroscopy in lithium-ion batteries. *J Power Sources* 2021;512:230508. <https://doi.org/10.1016/j.jpowsour.2021.230508>.
- [37] Brown DE, McShane EJ, Konz ZM, Knudsen KB, McCloskey BD. Detecting onset of lithium plating during fast charging of Li-ion batteries using operando electrochemical impedance spectroscopy. *Cell Rep Phys Sci* 2021;2(10):100589. <https://doi.org/10.1016/j.xcrp.2021.100589>.
- [38] Xu T, Peng Z, Liu D, Wu L. A hybrid drive method for capacity prediction of lithium-ion batteries. *IEEE Trans Transp Electr* 2022;8(1):1000–12.
- [39] Fu Y, Xu J, Shi M, Mei X. A fast impedance calculation based battery state-of-health estimation method. *IEEE Trans Ind Electron* 2022;69(7):7019–28.
- [40] Xiong R, Tian J, Mu H, Wang C. A systematic model-based degradation behavior recognition and health monitoring method for lithium-ion batteries. *Appl Energy* 2017;207:372–83.
- [41] Wang X, Wei X, Dai H. Estimation of state of health of lithium-ion batteries based on charge transfer resistance considering different temperature and state of charge. *J Energy Storage* 2019;21:618–31.
- [42] Luo F, Huang H, Ni L, Li T. Rapid prediction of the state of health of retired power batteries based on electrochemical impedance spectroscopy. *J Energy Storage* 2021;41:102866. <https://doi.org/10.1016/j.est.2021.102866>.
- [43] Messing M, Shoa T, Habibi S. Estimating battery state of health using electrochemical impedance spectroscopy and the relaxation effect. *J Energy Storage* 2021;43:103210. <https://doi.org/10.1016/j.est.2021.103210>.
- [44] Locorotondo E, Cultrera V, Pugi L, Berzi L, Pierini M, Lutzemberger G. Development of a battery real-time state of health diagnosis based on fast impedance measurements. *J Energy Storage* 2021;38:102566. <https://doi.org/10.1016/j.est.2021.102566>.
- [45] Jiang Bo, Dai H, Wei X. Incremental capacity analysis based adaptive capacity estimation for lithium-ion battery considering charging condition. *Appl Energy* 2020;269:115074. <https://doi.org/10.1016/j.apenergy.2020.115074>.
- [46] Horstkötter I, Gesner P, Hadler K, Bäker B. A phenomenological ageing study of lithium-ion batteries under dynamic loads. *J Energy Storage* 2021;42:102962. <https://doi.org/10.1016/j.est.2021.102962>.
- [47] Schimpe M, von Kuepach ME, Naumann M, Hesse HC, Smith K, Jossen A. Comprehensive modeling of temperature-dependent degradation mechanisms in Lithium iron phosphate batteries. *J Electrochem Soc* 2018;165(2):A181–93.
- [48] Andre D, Meiler M, Steiner K, Wimmer Ch, Soczka-Guth T, Sauer DU. Characterization of high-power lithium-ion batteries by electrochemical impedance spectroscopy. I Experimental investigation. *J Power Sources* 2011;196(12):5334–41.
- [49] Andre D, Meiler M, Steiner K, Walz H, Soczka-Guth T, Sauer DU. Characterization of high-power lithium-ion batteries by electrochemical impedance spectroscopy. II: modelling. *J Power Sources* 2011;196(12):5349–56.
- [50] Tian J, Xiong R, Shen W, Wang J. A Comparative study of fractional order models on state of charge estimation for Lithium ion batteries. *Chinese J Mechat Eng* 2020;33:51.
- [51] Zhu J, Dewi Darma MS, Knapp M, Sørensen DR, Heere M, Fang Q, et al. Investigation of lithium-ion battery degradation mechanisms by combining differential voltage analysis and alternating current impedance. *J Power Sources* 2020;448:227575. <https://doi.org/10.1016/j.jpowsour.2019.227575>.
- [52] Liu K, Ashwin TR, Hu X, Lucu M, Widanage WD. An evaluation study of different modelling techniques for calendar ageing prediction of lithium-ion batteries. *Renew Sustainable Energy Rev* 2020;131:110017. <https://doi.org/10.1016/j.rser.2020.110017>.
- [53] Liu K, Tang X, Teodorescu R, Gao F, Meng J. Future ageing trajectory prediction for Lithium-ion battery considering the knee point effect. *IEEE Trans Energy Convers* 2021;1–10.
- [54] Rasmussen CE, Nickisch H. Gaussian processes for machine learning (GPML) toolbox. *J Machine Learn Res* 2010;11:3011–5.
- [55] Eddahech A, Briat O, Woigard E, Vinassa JM. Remaining useful life prediction of lithium batteries in calendar ageing for automotive applications. *Microelectron Reliab* 2012;52(9–10):2438–42.
- [56] Xiao F, Li C, Fan Y, Yang G, Tang X. State of charge estimation for lithium-ion battery based on Gaussian process regression with deep recurrent kernel. *Int J*

- Electr Power Energy Syst 2021;124:106369. <https://doi.org/10.1016/j.ijepes.2020.106369>.
- [57] Roman D, Saxena S, Robu V, Pecht M, Flynn D. Machine learning pipeline for battery state-of-health estimation. *Nat Mach Intell* 2021;3(5):447–56.
- [58] Sui X, He S, Vilsen SB, Meng J, Teodorescu R, Stroe D-I. A review of non-probabilistic machine learning-based state of health estimation techniques for Lithium-ion battery. *Appl Energy* 2021;300:117346. <https://doi.org/10.1016/j.apenergy.2021.117346>.
- [59] Zhang Y, Li Y-F. Prognostics and health management of Lithium-ion battery using deep learning methods: a review. *Renew Sustainable Energy Rev* 2022;161:112282. <https://doi.org/10.1016/j.rser.2022.112282>.
- [60] Hossain Lipu MS, Hannan MA, Hussain A, Ayob A, Saad MHM, Karim TF, et al. Data-driven state of charge estimation of lithium-ion batteries: algorithms, implementation factors, limitations and future trends. *J Cleaner Prod* 2020;277:124110. <https://doi.org/10.1016/j.jclepro.2020.124110>.
- [61] Yang S, Zhang C, Jiang J, Zhang W, Zhang L, Wang Y. Review on state-of-health of lithium-ion batteries: characterizations, estimations and applications. *J Cleaner Prod* 2021;314.